Title

Soft X-ray spectroscopy of nanoparticles by velocity map imaging

Journal
The Journal of Chemical Physics, 147(1)

ISSN
0021-9606

Authors

Kostko, O
Xu, B
Jacobs, MI
et al.

Publication Date
2017-07-07

DOI
10.1063/1.4982822

Peer reviewed

Soft X-ray spectroscopy of nanoparticles by velocity map imaging

O. Kostko,[1] B. Xu,[1] M. I. Jacobs,[1,2] and M. Ahmed[1]

[1] Chemical Sciences Division, Lawrence Berkeley National Laboratory, Berkeley, CA 94720 (USA)

[2] Department of Chemistry, University of California, Berkeley, CA 94720 (USA)

ABSTRACT

Velocity map imaging (VMI), a technique traditionally used to study chemical dynamics in the gas phase, is applied here to study X-ray photoemission from aerosol nanoparticles. Soft X-rays from the Advanced Light Source synchrotron probe a beam of nanoparticles, and the resulting photoelectrons with 0-100 eV kinetic energy are velocity mapped to obtain their kinetic energy and angular distributions. The experimental apparatus is benchmarked by measuring vacuum ultraviolet (VUV) photoemission from gas phase xenon and squalene nanoparticles followed by measurements using soft X-rays. The photoelectron distribution from X-ray irradiated squalene nanoparticles is dominated by secondary electrons. By scanning the photon energies and measuring the intensities of these secondary electrons, a near edge X-ray absorption fine structure (NEXAFS) spectrum is obtained. The NEXAFS technique is used to study aqueous nanoparticles at the O K edge. By varying the position of the aqueous nanoparticle beam relative to the incident X-ray beam, evidence is presented that the VMI technique allows for NEXAFS spectroscopy of gaseous, liquid, and ice water. Finally we discuss the possibility of applying VMI methods to probe liquids and solids via X-ray spectroscopy.

INTRODUCTION

Photoemission is an extremely powerful method that probes the electronic structure of complex molecules. From its initial use in probing of electronic structure of freshly cleaved single crystals in an ultra-high vacuum environment to its current application to systems relevant to electrochemistry, catalysis and interfacial science, the photoemission field has matured considerably over the last half century. When coupled with tunable photon sources, the technique allows for probing systems that have not been traditionally accessible.

A current topic of interest is the probing of chemistry in aqueous systems with photoemission. However, the high vapor pressure of liquid water makes operating in a traditional high vacuum environment nearly impossible, and also leads to scattering losses of the emitted electrons. A popular approach to overcome this problem is to reduce the surface area of the liquid which minimizes evaporation of water molecules. Current implementations of this approach include: liquid microjet, microdroplets, and aerosols. One successful approach to deal with the high vapor pressure of the solvent is to improve the differential pumping scheme of the electron analyzer and move it closer to the probing region. This was started by Siegbahn and Siegbahn[1] in 1970s and first implemented at a synchrotron light source by Bluhm, Salmeron and coworkers.[2,3]

The pioneering work of Faubel et al. on the implementation of VUV photoelectron spectroscopy on liquid microjets[4] led to studies on the electronic structure of liquids and solvated molecules, including pure water[4,5] and solvated biomolecules.[6] Recently, liquid microjets have been used in novel regimes, such as probing the solid-liquid interface using nanoparticles dissolved in a solvent.[7–10] Both X-ray photoelectron spectroscopy (XPS)—using hemispherical energy analyzers—and NEXAFS spectroscopy[11,12] have been applied to liquid microjets. The microdroplet probing technique is a modification of the liquid microjet experiment. The liquid jet can be split into a highly uniform droplet train which can be probed via ambient pressure XPS[13] or NEXAFS spectroscopy techniques. Though the approach has some advantages over the liquid jet technique it has not received wide application.

Ahmed, Wilson and co-workers pioneered the implementation of photoelectron spectroscopy of unsupported, gas-phase aerosols by using an aerodynamic lens for particle focusing coupled to a velocity map imaging (VMI) spectrometer. These first experiments, performed over a decade ago, were conducted on both inorganic[14–16] and organic[17] aerosol using tunable synchrotron VUV radiation. The technique of photoelectron spectroscopy of aerosol nanoparticles has been subsequently applied to the investigation of various systems. For example, an aerodynamic lens coupled to a hemispherical analyzer was used to perform valence band photoelectron spectroscopy of aqueous aerosols of biomolecules, which observed changes in the charge-transfer mechanism at different pH conditions of a solvent.[18,19] A similar setup has been used at synchrotron SOLEIL to investigate solid silicon[20] and flame generated nanoparticles (soot)[21] by means of XPS and NEXAFS. The spectroscopies performed at the carbon 1s edge compared the oxidation states of the surface (detected by XPS) and bulk (shown by NEXAFS) of soot nanoparticles.[21] The group of Signorell has begun a series of studies using tunable synchrotron, lab based VUV radiation, and multiphoton ionization to extract electron mean free path of low energy electrons using a VMI spectrometer coupled to an aerodynamic lens system.[22,23] A VMI spectrometer coupled to an aerodynamic lens and ultrafast laser was used to understand the interaction of intense laser fields with isolated nanoparticles. The interaction of attosecond laser pulses with SiO_2 nanoparticles inside of a VMI spectrometer visualized the collective electron motion in unsupported nanoparticles.[24] Another technique, termed “plasma explosion imaging”, was used to study the absorption of strong femtosecond laser fields by isolated nanoparticles. In this case, ions generated after a nanoparticle absorbs a strong femtosecond pulse were velocity map imaged.[25]

VMI photoelectron spectroscopy of aerosols has numerous advantages over conventional photoelectron spectroscopy. For example, the absorption of a single photon per nanoparticle leads to the probing of a fresh nanoparticle surface. Additionally, single photon absorption limits the charging problem which is common in surface XPS. An added advantage of VMI spectroscopy is the collection of 4π distribution of emitted electrons, compared to the limited solid angle electron acceptance in hemispherical electron analyzers. Nevertheless, VMI spectrometers are constrained by their ability to accept electrons with kinetic energy from zero to a finite maximum which limits access to high kinetic energy electrons as well as limits energy resolution.

In this paper, we present the first implementation of X-ray photoelectron and NEXAFS spectroscopies of unsupported gas-phase nanoparticles by velocity map imaging technique. We also discuss several possible applications to study organic nanoparticles, biomolecules in aqueous environment and possibilities for the investigation of aqueous systems.

EXPERIMENTAL METHODS

The photoelectron spectrometer was designed to detect electrons with kinetic energy up to 100 eV and also to accommodate different types of samples: gas-phase molecules and unsupported nanoparticles. The final implementation of the experimental apparatus is shown in Fig. 1a. The apparatus consists of an aerodynamic lens with two differential pumping regions (Fig. 1a, left) and a VMI photoelectron spectrometer (Fig. 1a, right).

The size of the imaging detector (Photonis PS32405, diameter of the active zone is 75 mm) and the highest practical voltage (8 kV) preset most of the remaining dimensions of the spectrometer. To be able to detect electrons with kinetic energy of 100 eV, the VMI electron optics need to be relatively compact. A four electrode scheme was chosen to provide additional flexibility (Fig. 1b). The electrode El4 serves as a repeller, El3 - extractor, El2 - lens, and electrode El1 has a ground potential, which is the same as front of the detector. Compared to the classic three electrode scheme,[26] the additional electrode El2 provides the possibility to improve the resolution of the spectrometer.

Simion 8.0 was used to design the final dimensions and positions of the VMI electrodes. The scripting functionality of Simion was utilized to automate the simulations. This consisted of changing dimensions and positions of electrodes, generating a new ion optics geometry file, applying different voltages to the electrodes, and detecting positions of the electrons at the detector. The electrons were emitted at different angles to the vertical axis of the VMI optics and from slightly different initial positions (Fig. 1c). The spread between the positions of electrons which should collide with a detector at the same location was used to determine the resolution of the spectrometer using the following relation:

$$\frac{\Delta KE}{KE} \cong \frac{2\Delta R}{R}, \qquad (1)$$

where *KE* is the initial electron kinetic energy, *R* is the distance from the center of a detector to where the electron collision takes place, *ΔKE* and *ΔR* are the corresponding spreads in kinetic energy and distance. The best resolution of the spectrometer (*ΔKE/KE*) of 1.0 % was obtained in the simulations with the following geometries: a 220 mm length between the interaction region and the detector; and 80 mm, 70 mm, and 100 mm openings in electrodes El1, El2, and El3, respectively. To obtain a better picture of the spectrometer resolution, a more complex 3D model of the spectrometer was constructed in the Simion software and 100,000 electrons with kinetic energy ranging from 10 to 100 eV in 10 eV increments were emitted from the interaction region. The electrons had a Gaussian spread of both their initial positions around the interaction region and their initial kinetic energies, and a random distribution of the initial directions. The simulation resulted in an image similar to the one obtained by the spectrometer's camera. This image was reconstructed using the same techniques that are applied to the experimental data. The resolution of the spectrometer obtained from the 3D simulation was energy dependent (resolution was better for higher KE) and was 1.2 % for 80 eV KE.

The final design based on the simulation is shown in Fig. 1b. Each electrode has a side protection to avoid perturbation of the electric field inside of the spectrometer by external electric fields, such as those generated by voltage leads. The electrodes are mounted on four plastic isolators that support the whole construction. The VMI optics is protected from magnetic fields by a cylindrical mu-metal shield, placed outside of plastic electrode holders. Electrode El4 has a large opening covered by a metal mesh which reduces the number of background electrons generated by scattered light. The plate below El4 (Fig. 1b) is used to attach a nozzle, supplying gas-phase samples or an oven to vaporize and introduce solid samples.

Electrons that reach the detector are amplified by dual micro-channel plates and hit a fast phosphor (P47) screen. The light generated by the electrons hitting the phosphor screen is detected by a camera with a CMOS sensor (Teledyne Dalsa Genie model TS-2048) coupled to a 25 mm fixed focal length lens. Images, acquired by the camera are transferred to a PC via a network cable and accumulated by a LabVIEW program. The data is collected as two images: a signal image with sample present in the interaction region and a background image without sample present in the interaction region. The difference between the two represents the image of electrons emitted by the sample. For reconstruction of the obtained images, two different algorithms were applied: BASEX[27] and pBASEX.[28]

A system for the delivery of gas-phase nanoparticles is attached to the VMI photoelectron spectrometer chamber and consists of an aerodynamic lens coupled to two differential pumping regions (DPR1 and DPR2 in Fig. 1a). The differential pumping regions are needed to reduce pressure from atmospheric before the inlet of the ADL to 10^{-6} Torr inside of the VMI chamber. The aerodynamic lens was designed using an aerodynamic lens calculator.[29,30] A gas flow limiting aperture of 100-200 µm diameter is used as an inlet of the aerodynamic lens.

Nanoparticles are either generated via homogeneous nucleation or atomizing solutions. For homogeneous nucleation, nanoparticles are generated by passing dry nitrogen over a heated reservoir (150 °C) containing the pure compound of interest (squalene in this case). The cooling obtained as the flow leaves the oven, causes nanoparticles to nucleate. The size distributions of the nanoparticles are measured using a scanning mobility particle sizer (TSI, Model 3080). The diameters of the squalene nanoparticle are log-normal in distribution with an average diameter of ~220±40 nm. To generate aqueous nanoparticles of water, solutions are atomized using a high flux atomizer (TSI, Model 3076). The size distribution of aqueous nanoparticles is broad, with the average diameter around 100 nm.

RESULTS

The performance of the VMI apparatus was tested on various samples using tunable synchrotron radiation generated by beamlines 6.0.2, 6.3.2, 9.0.2, and 11.0.2 of the Advanced Light Source, Lawrence Berkeley National Laboratory. The VMI image collected by the apparatus for gaseous xenon sample utilizing 22 eV VUV photons is shown in Figure 2a. The two rings in Fig. 2a correspond to the Xe $5p_{1/2}$ (inner ring, kinetic energy of 8.6 eV) and $5p_{3/2}$ (outer ring, kinetic energy of 9.9 eV) lines. The VMI image of xenon collected with photon energy of 80 eV also demonstrates a double ring (feature 1 in Figure 2b), which in this case corresponds to emission of $4d_{3/2}$ (inner ring) and $4d_{5/2}$ (outer ring) electrons with kinetic energies of 10.5 eV and 12.5 eV, respectively. Another noticeable feature (labeled by 2 in Fig. 2b) is an additional ring of larger diameter and higher kinetic energy electrons, which has a lower intensity than that of the double ring. Its diameter is photon energy independent. The ring corresponds to the Auger $N_{4,5}O_{2,3}O_{2,3}$ decay of 4*d* holes, created during photoionization. The kinetic energy of Auger electrons within this feature lies in a range of 30-35 eV and correlates well with the literature data.[31,32] Two additional bright rings in the center of the image, labeled 3 in Fig. 2b are due to Xe 4*d* double Auger decay: sequential decay of holes generated in a primary Auger process. The double Auger process results in two rings, which correspond to electrons with kinetic energy of 1.6 and 3.5 eV. Again, this correlates well with previous observations.[33,34] Feature 4 in Figure 2b is due to the edge of the imaging detector. The photoelectron spectrum reconstructed from the image using pBASEX algorithm is shown in Fig. 3a.

VMI images of squalene nanoparticles measured using VUV (15 eV) and X-ray (315 eV) radiation are shown in Figures 2c and 2d, respectively. The shallow penetration depth of VUV photons of less than 10 nm leads to preferential ionization and subsequent emission of electrons from the side of the nanoparticle directed toward the source of light. This image asymmetry observed in Figure 2c is caused by strong VUV light attenuation and was observed previously.[14,22,23] X-ray photons in contrary have a larger light attenuation distance on the order of microns, which results in equal possibility of ionization of any molecule within a nanoparticle and leads to a symmetrical image (Fig. 2d). Feature 1 in Figure 2d corresponds to carbon 1*s* electrons emitted by squalene nanoparticles after absorption of 315 eV photons. The kinetic energy of the emitted C 1*s* electrons is 26.7 eV in this case.

A large, bright, and symmetrical spot in the center of Fig. 2d appears due to emission of secondary electrons, which are commonly observed in XPS measurements of bulk materials.[35] Absorption of an X-ray photon by a nanoparticle leads to photoionization and emission of a C 1*s* electron (emission of a valence electron has lower probability due to significantly lower photoionization cross-section). A hole left after the emission of an electron may decay via *KLL* Auger process (which for carbon is a far more dominant process than the fluorescence)[36] leading to the emission of a second electron with kinetic energy of 264 eV.[37] Inelastic collisions of the energetic Auger electron (as well as of the photoelectron) with surrounding electrons will lead to emission of additional (secondary) electrons and reduction of kinetic energy of colliding primary (Auger or photo-) electrons. The corresponding reconstructed photoelectron spectrum generated from the image (Fig. 2d) is shown in Fig. 3b. The spectrum demonstrates two pronounced features: a narrow, Gaussian-shaped peak at kinetic energy of 26.7 eV and a fast-rising and exponentially decaying broad feature, peaking at 2.5-3.0 eV. The former peak corresponds to a C 1*s* squalene photoelectrons, the latter is a broad secondary electron distribution.

A theoretical model developed by Henke et al. in the early era of X-ray photoelectron spectroscopy[38] was applied to fit the experimental distribution of secondary electrons observed in Fig. 3b. The theoretical model assumes that the primary (photo- and Auger) electrons are responsible for generation of secondary electrons and it takes into account both electron-electron and electron-phonon scattering during electron transport inside of solids. The function proposed to fit secondary electron emission spectrum from semiconductors and insulators is:

$$I(E_K) = k\,\frac{E_K}{(E_K+E_A)^3}\,, \tag{2}$$

where I is the energy dependent signal intensity, k is a fitting coefficient, E_K is electron kinetic energy, and E_A is the electron affinity energy. A similar formula was proposed by Henke et al. for modeling electron emission from metals, but with the denominator raised to the fourth power instead of the third power and the electron affinity replaced with a work function.[39] The fit of the experimental data shown in Fig. 3b results in an E_A of 4.4 eV, which is above any of known atomic electron affinities. The electron affinity energy is included in the theoretical model as the energy reducing the kinetic energy of an electron, when it crosses a barrier between solid and vacuum. The high value of the E_A suggests that in the case of a spherical nanoparticle, there is an additional barrier, strongly reducing the kinetic energy of escaping electrons. The high value could also arise from a different geometry of a photoelectron spectrometer used in the case of Henke et al. compared to a VMI system.

The C 1s photoelectron peak in Fig. 3b is fit by a Gaussian function with FWHM of 1.27 eV. The VMI spectrometer energy resolution $\Delta KE/KE$ is 4.7 %, which is 2.4 times larger than the value found in the 3D Simion model of the VMI electron optics (2.0 % at kinetic energy of 25 eV).

From an analysis of the reconstructed photoelectron spectrum (Fig. 3b), it becomes obvious that the secondary electron signal dominates the spectrum and is many times stronger than the primary photoelectron peak. A similar behavior is observed in conventional photoelectron spectroscopy of bulk samples, where the majority (from 50 to 90% according to Henke et al.[39]) of emitted electrons have kinetic energy ranging from 0 to 30 eV.

Total electron yield is a common NEXAFS detection technique that measures X-ray absorption of a material by detecting the emitted electrons with all kinetic energies.[40] These measured electrons are dominated by low kinetic energy secondary electrons that are similar to those observed here in the VMI spectra of nanoparticles. Therefore, by measuring the dependence of secondary electron intensity vs. excitation photon energy, a NEXAFS spectrum of unsupported nanoparticles can be obtained using a VMI spectrometer.

Two different approaches were used to collect a NEXAFS spectrum using a VMI spectrometer. In the first approach, the NEXAFS spectra were collected by a camera, in the same way as photoelectron spectra. However, because of the high secondary electron signal intensity, the NEXAFS images can be collected in less time than the photoelectron spectra with acceptable signal to noise ratio. The intensity of the NEXAFS signal was extracted by finding a sum of separate pixel intensities in the central part of the velocity-map image. Another much faster technique used a photomultiplier tube instead of a camera. The tube collected only signal from the central part of the image and was dominated by low energy secondary electrons. Because of the additional signal amplification in the photomultiplier tube, the duration of signal collection at a single photon energy could be as small as one second, compared to 5-10 seconds in case of camera accumulation. NEXAFS spectra collected by both techniques are compared in Figure 3c and are similar in shape.

DISCUSSION

XPS and NEXAFS techniques complement each other. XPS is a very surface sensitive technique due to the short inelastic mean free path (IMFP) of electrons. The so-called “universal curve”, which depicts the energy dependence of the IMFP of electrons, has a minimum around 50-100 eV kinetic energy, corresponding to an IMFP of 0.5-1 nm.[41] For lower kinetic energy electrons, the universal curve exhibits higher values of IMFP, but there is an active discussion about the IMFP behavior at these energies.[5] Using photon energies that lead to emission of electrons with kinetic energies ranging from 50 to 100 eV, XPS provides information on the electronic structure of the surface. Reducing the photon energy (which corresponds to a decrease in the kinetic energy of emitted electron) leads to a larger probing depth. Thus, in contrast to XPS, NEXAFS spectroscopy is more depth sensitive, as it collects mostly low kinetic energy secondary electrons with larger IMFP.

Recently the described techniques were applied to investigate kinetics of the ozonolysis of squalene nanoparticles.[42] The X-ray photoelectron spectroscopy was able to resolve peaks at C 1*s* edge corresponding to differently bound carbon, such as: C=C, CHx, C-O, and C=O bonds. The kinetics of the ozonolysis reaction were extracted from the analysis of C=C peak decay with increased ozone exposure. A similar result was obtained from a NEXAFS measurement at the C and O K edges. In this particular case XPS and NEXAFS measurements resulted in similar uptake coefficients despite the different probing depths of the methods. This is explained by the fact that squalene is a well-mixed liquid with a homogeneous composition.

Below we discuss the possibility of using X-ray photoelectron and NEXAFS spectroscopies on unsupported nanoparticles for analysis of more complex systems such as liquids and solvated biomolecules. It is difficult to couple a liquid jet to a VMI spectrometer because of the close proximity of a high vapor pressure liquid to a pressure sensitive electron detector. However, nanoparticles generated from a solution of biomolecules passing through an aerodynamic lens, have been studied via photoelectron spectroscopy,[18] providing information of electronic structure of biomolecules in a liquid environment.

A NEXAFS spectrum at the O K edge of aerosol nanoparticles generated from pure water is shown in Fig. 4a. A small addition of NaI to water (0.038 M) changes the spectrum shape; the post-edge feature located around 541 eV becomes less intense (Fig. 4b). The NEXAFS spectrum of gas-phase water (Fig. 4c) is collected by moving the nanoparticle beam ~1 mm below the probing region. Though water nanoparticles are still present in the VMI spectrometer in this case, they do not interact with the X-ray beam, and the observed signal arises from the gas-phase water molecules that have evaporated from the particles. A good correlation of the current measurement to the previous data[43] is observed for gas-phase water in Fig. 4c.

The pre-, main-, and post- edge features observed in the water NEXAFS spectra are explained by different coordination of the H-bonding network. The pre-edge feature corresponds to weakened/nonexistent hydrogen bonding and to less coordinated water molecules. It is generally associated with the liquid state. The post-edge feature corresponds to the fully coordinated H-bonding network. The enhancement of tetrahedral coordination, observed in ice, leads to increase of the post-edge NEXAFS feature (and decrease of pre-edge signal).[43] In the measured NEXAFS spectra, the post-edge feature intensity is stronger for nanoparticles generated from pure water than for nanoparticles from 0.038 M NaI solution. Such changes in the NEXAFS spectra have been observed during changes in temperature (physical state) of water and upon introduction of solutes.

As described earlier, the decrease of water temperature leads to increase of the post-edge peak and decrease of the pre-edge feature. This dependence has been experimentally observed previously for both liquid water and ice (see e.g. Refs. [44–46]). The temperature of an aerosol in the VMI spectrometer is less defined than that in a liquid jet experiment. The aerosol nanoparticles are much smaller than the diameter of a liquid jet (hundreds of nanometers vs. ~10 microns) and, because of the differential pumping in the spectrometer, they travel a longer distance to the interaction region, which leads to extended evaporative cooling. According to estimates of Chang et al. glutathione-water aerosol nanoparticles could be in a deeply supercooled state, residing at ~193 K in the interaction region.[19] However, despite the very low temperature of the aerosol nanoparticles, the authors claim that spectral features characteristic of liquid water are observed. Electron diffraction measurements conducted on the supercooled water nanodroplets revealed existence of a liquid phase at temperatures as low as 200 K.[47] However, more recent coherent X-ray scattering measurements on micrometer sized water droplets demonstrated a slightly larger liquid-ice transition point of 227 K, at which a tiny portion of droplets still remained liquid.[48]

The NEXAFS spectrum of pure water aerosol nanoparticles in Fig. 4a cannot be fit well by either liquid water or ice. The NEXAFS spectrum of liquid water has a stronger and better resolved pre-edge feature and less intense post-edge peak than that observed in Fig. 4a, whereas the spectrum of ice has a smaller pre-edge and a stronger post-edge feature.[45] The spectrum in Fig. 4a could be fit by a linear combination of 40 % liquid water and 60 % ice NEXAFS spectra obtained from Ref. [43]. This coexistence of liquid and ice nanoparticles could be a result of the broad size distribution (50 – 700 nm) of water nanoparticles used in the current experiment, which will lead to different cooling rates and temperatures of the nanoparticles in the probed region, some of which may remain liquid. The spectrum of 0.038 M aqueous solution of NaI (Fig. 4b) correlates well with pure water in the pre- and main-edges and has a substantially lower intensity of post-edge peak. Below we attempt to explain the observed deviation.

Addition of salt to water depresses the freezing point of a solution. For the low NaI concentration used, the freezing point depression (ΔT) can be estimated from a Blagden's law, which results in ΔT = 0.14 K. This negligible decrease of freezing temperature cannot significantly affect a physical state of aerosol, though preferential removal of water molecules during evaporative cooling may lead to a slight increase of sodium and iodine ion concentrations in the nanoparticles.

Another effect of NaI addition is the interaction of the resultant ions with surrounding water molecules. It was observed that the shape of the O K edge NEXAFS spectrum of water changes with the addition of salts, with changes progressing as the salt concentration increases.[49,50] Similar changes are also observed in vibrational sum-frequency spectroscopy.[51] These changes are interpreted as iodine anions (which show a propensity for the interface)[52] weakening the water bonding coordination network near the surface region. The influence of the dissolved ions on the coordination of the water molecules in bulk water is still a subject of active discussion.[50,53–55] The observed reduction of the post-edge feature with the addition of NaI (Fig. 4b) could be rationalized as an increased concentration of iodide anions in the surface layer leading to a perturbation of the tetrahedral coordination of water molecules. A Raman thermometry setup, similar to that used in ref. [56] (measuring temperature of a liquid jet) is underway to quantify the aerosol temperature .

Finally, we note that the VMI technique could be extended to study stationary liquids and surfaces, with the intentions of probing chemical reactions, solvation, photochemistry or electrochemistry. There have been several approaches to study solid samples within a VMI spectrometer. Ions generated by post-desorption ionization were imaged using a VMI spectrometer and their velocities and distributions were studied.[57,58] It was found that a VMI spectrometer can also be used to measure the kinetic energy distribution of electrons emitted from a small solid target (e.g. a metal tip) inside of a VMI spectrometer after interaction of the target with femtosecond laser radiation.[59,60] With proper modification of a VMI spectrometer, it should be possible to collect electrons emitted from a conductive surface. Additionally, a liquid meniscus from a small orifice (2-5 microns) in a SiN thin film has been formed and probed in an UHV environment. Ions from this liquid surface were directly probed using secondary ion mass spectrometry.[61] We are currently implementing this device within our VMI spectrometer to perform photoelectron spectroscopy of liquids.

CONCLUSIONS

This study describes a velocity map imaging photoelectron spectrometer and its application for X-ray photoemission experiments on unsupported nanoparticles. The photoelectron spectrometer, capable of collecting electrons with kinetic energy up to 100 eV, was commissioned using tunable synchrotron radiation and gas phase samples. X-ray photoelectron spectra of organic nanoparticles measured at carbon K-edge demonstrated a strong low kinetic energy background explained as emission of secondary electrons caused by inelastic scattering of Auger electrons. It is demonstrated that the signal of the low kinetic energy secondary electrons can be used to perform NEXAFS spectroscopy of unsupported nanoparticles. NEXAFS spectra of water nanoparticles, prepared from pure water, 0.038 M NaI solution and of gas-phase water molecules are presented. The observed spectral features are explained in terms of coexisting frozen and liquid nanoparticles and perturbation of tetrahedral molecular coordination by iodide anions in a surface layer of nanoparticles prepared from NaI solution. Finally, we provide a brief outlook on applications of VMI for investigation of liquids and solutions.

ACKNOWLEDGEMENTS

This work and the Advanced Light Source are supported by the Director, Office of Science, Office of Basic Energy Sciences, of the U.S. Department of Energy under Contract No. DE-AC02-05CH11231, through the Chemical Sciences Division. M.I.J. thanks the NSF for an NSF Graduate Research Fellowship under DGE-1106400. O.K. is thankful to Kevin R. Wilson and Hendrik Bluhm for fruitful discussions. Authors acknowledge help of Elio Champenois, developed Matlab and Python implementations of pBASEX code used in the current paper.[62]

REFERENCES

[1] H. Siegbahn and K. Siegbahn, J. Electron Spectrosc. Relat. Phenom. **2**, 319 (1973).

[2] D.F. Ogletree, H. Bluhm, G. Lebedev, C.S. Fadley, Z. Hussain, and M. Salmeron, Rev. Sci. Instrum. **73**, 3872 (2002).

[3] D.E. Starr, Z. Liu, M. Hävecker, A. Knop-Gericke, and H. Bluhm, Chem. Soc. Rev. **42**, 5833 (2013).

[4] M. Faubel, B. Steiner, and J.P. Toennies, J. Chem. Phys. **106**, 9013 (1997).

[5] S. Thürmer, R. Seidel, M. Faubel, W. Eberhardt, J.C. Hemminger, S.E. Bradforth, and B. Winter, Phys. Rev. Lett. **111**, 173005 (2013).

[6] N. Ottosson, K.J. Børve, D. Spångberg, H. Bergersen, L.J. Sæthre, M. Faubel, W. Pokapanich, G. Öhrwall, O. Björneholm, and B. Winter, J. Am. Chem. Soc. **133**, 3120 (2011).

[7] M.A. Brown, I. Jordan, A. Beloqui Redondo, A. Kleibert, H.J. Wörner, and J.A. van Bokhoven, Surf. Sci. **610**, 1 (2013).

[8] M.A. Brown, R. Seidel, S. Thürmer, M. Faubel, J.C. Hemminger, J.A. van Bokhoven, B. Winter, and M. Sterrer, Phys. Chem. Chem. Phys. **13**, 12720 (2011).

[9] J. Söderström, N. Ottosson, W. Pokapanich, G. Öhrwall, and O. Björneholm, J. Electron Spectrosc. Relat. Phenom. **184**, 375 (2011).

[10] M.J. Makowski, R.P. Galhenage, J. Langford, and J.C. Hemminger, J. Phys. Chem. Lett. **7**, 1732 (2016).

[11] B.M. Messer, C.D. Cappa, J.D. Smith, K.R. Wilson, M.K. Gilles, R.C. Cohen, and R.J. Saykally, J. Phys. Chem. B **109**, 5375 (2005).

[12] D. Nolting, E.F. Aziz, N. Ottosson, M. Faubel, I.V. Hertel, and B. Winter, J. Am. Chem. Soc. **129**, 14068 (2007).

[13] D.E. Starr, E.K. Wong, D.R. Worsnop, K.R. Wilson, and H. Bluhm, Phys. Chem. Chem. Phys. **10**, 3093 (2008).

[14] K.R. Wilson, S. Zou, J. Shu, E. Rühl, S.R. Leone, G.C. Schatz, and M. Ahmed, Nano Lett. **7**, 2014 (2007).

[15] M.J. Berg, K.R. Wilson, C.M. Sorensen, A. Chakrabarti, and M. Ahmed, J. Quant. Spectrosc. Radiat. Transf. **113**, 259 (2012).

[16] J. Shu, K.R. Wilson, M. Ahmed, and S.R. Leone, Rev. Sci. Instrum. **77**, 043106 (2006).

[17] K.R. Wilson, D.S. Peterka, M. Jimenez-Cruz, S.R. Leone, and M. Ahmed, Phys. Chem. Chem. Phys. **8**, 1884 (2006).

[18] C.-C. Su, Y. Yu, P.-C. Chang, Y.-W. Chen, I.-Y. Chen, Y.-Y. Lee, and C.C. Wang, J. Phys. Chem. Lett. **6**, 817 (2015).

[19] P.-C. Chang, Y. Yu, Z.-H. Wu, P.-C. Lin, W.-R. Chen, C.-C. Su, M.-S. Chen, Y.-L. Li, T.-P. Huang, Y.-Y. Lee, and C.C. Wang, J. Phys. Chem. B **120**, 10181 (2016).

[20] O. Sublemontier, C. Nicolas, D. Aureau, M. Patanen, H. Kintz, X. Liu, M.-A. Gaveau, J.-L. Le Garrec, E. Robert, F.-A. Barreda, A. Etcheberry, C. Reynaud, J.B. Mitchell, and C. Miron, J. Phys. Chem. Lett. **5**, 3399 (2014).

[21] F.-X. Ouf, P. Parent, C. Laffon, I. Marhaba, D. Ferry, B. Marcillaud, E. Antonsson, S. Benkoula, X.-J. Liu, C. Nicolas, E. Robert, M. Patanen, F.-A. Barreda, O. Sublemontier, A. Coppalle, J. Yon, F. Miserque, T. Mostefaoui, T.Z. Regier, J.-B.A. Mitchell, and C. Miron, Sci. Rep. **6**, 36495 (2016).

[22] M. Goldmann, J. Miguel-Sánchez, A.H.C. West, B.L. Yoder, and R. Signorell, J. Chem. Phys. **142**, 224304 (2015).

[23] R. Signorell, M. Goldmann, B.L. Yoder, A. Bodi, E. Chasovskikh, L. Lang, and D. Luckhaus, Chem. Phys. Lett. **658**, 1 (2016).

[24] S. Zherebtsov, T. Fennel, J. Plenge, E. Antonsson, I. Znakovskaya, A. Wirth, O. Herrwerth, F. Süßmann, C. Peltz, I. Ahmad, S.A. Trushin, V. Pervak, S. Karsch, M.J.J. Vrakking, B. Langer, C. Graf, M.I. Stockman, F. Krausz, E. Rühl, and M.F. Kling, Nat. Phys. **7**, 656 (2011).

[25] D.D. Hickstein, F. Dollar, J.L. Ellis, K.J. Schnitzenbaumer, K.E. Keister, G.M. Petrov, C. Ding, B.B. Palm, J.A. Gaffney, M.E. Foord, S.B. Libby, G. Dukovic, J.L. Jimenez, H.C. Kapteyn, M.M. Murnane, and W. Xiong, ACS Nano **8**, 8810 (2014).
[26] A.T.J.B. Eppink and D.H. Parker, Rev. Sci. Instrum. **68**, 3477 (1997).
[27] V. Dribinski, A. Ossadtchi, V.A. Mandelshtam, and H. Reisler, Rev. Sci. Instrum. **73**, 2634 (2002).
[28] G.A. Garcia, L. Nahon, and I. Powis, Rev. Sci. Instrum. **75**, 4989 (2004).
[29] X. Wang and P. McMurry, Aerosol Sci. Technol. **40**, 320 (2006).
[30] X. Wang and P.H. McMurry, Aerosol Sci. Technol. **40**, 1 (2006).
[31] S. Ohtani, H. Nishimura, H. Suzuki, and K. Wakiya, Phys. Rev. Lett. **36**, 863 (1976).
[32] A. Kivimäki, L. Pfeiffer, H. Aksela, E. Nõmmiste, and S. Aksela, J. Electron Spectrosc. Relat. Phenom. **101**–**103**, 43 (1999).
[33] J. Viefhaus, M. Braune, S. Korica, A. Reinköster, D. Rolles, and U. Becker, J. Phys. B At. Mol. Opt. Phys. **38**, 3885 (2005).
[34] F. Penent, J. Palaudoux, P. Lablanquie, L. Andric, R. Feifel, and J.H.D. Eland, Phys. Rev. Lett. **95**, 083002 (2005).
[35] P.D.S. Hüfner, in *Photoelectron Spectrosc.* (Springer Berlin Heidelberg, 1996), pp. 1–26.
[36] M.O. Krause, J. Phys. Chem. Ref. Data **8**, 307 (1979).
[37] J.F. Moulder, W.F. Stickle, P.E. Sobol, and K.D. Bomben, *Handbook of X-Ray Photoelectron Spectroscopy* (Physical Electronics, Inc., 1995).
[38] B.L. Henke, J. Liesegang, and S.D. Smith, Phys. Rev. B **19**, 3004 (1979).
[39] B.L. Henke, J.A. Smith, and D.T. Attwood, J. Appl. Phys. **48**, 1852 (1977).
[40] J. Stohr, *NEXAFS Spectroscopy* (Springer Berlin Heidelberg, 1996).
[41] M.P. Seah and W.A. Dench, Surf. Interface Anal. **1**, 2 (1979).
[42] M.I. Jacobs, B. Xu, O. Kostko, N. Heine, M. Ahmed, and K.R. Wilson, J. Phys. Chem. A **120**, 8645 (2016).
[43] T. Fransson, Y. Harada, N. Kosugi, N.A. Besley, B. Winter, J.J. Rehr, L.G.M. Pettersson, and A. Nilsson, Chem. Rev. **116**, 7551 (2016).
[44] T. Pylkkänen, A. Sakko, M. Hakala, K. Hämäläinen, G. Monaco, and S. Huotari, J. Phys. Chem. B **115**, 14544 (2011).
[45] J.A. Sellberg, S. Kaya, V.H. Segtnan, C. Chen, T. Tyliszczak, H. Ogasawara, D. Nordlund, L.G.M. Pettersson, and A. Nilsson, J. Chem. Phys. **141**, 034507 (2014).
[46] H. Bluhm, D.F. Ogletree, C.S. Fadley, Z. Hussain, and M. Salmeron, J. Phys. Condens. Matter **14**, L227 (2002).
[47] L.S. Bartell and J. Huang, J. Phys. Chem. **98**, 7455 (1994).
[48] J.A. Sellberg, C. Huang, T.A. McQueen, N.D. Loh, H. Laksmono, D. Schlesinger, R.G. Sierra, D. Nordlund, C.Y. Hampton, D. Starodub, D.P. DePonte, M. Beye, C. Chen, A.V. Martin, A. Barty, K.T. Wikfeldt, T.M. Weiss, C. Caronna, J. Feldkamp, L.B. Skinner, M.M. Seibert, M. Messerschmidt, G.J. Williams, S. Boutet, L.G.M. Pettersson, M.J. Bogan, and A. Nilsson, Nature **510**, 381 (2014).
[49] Y.L. Jeyachandran, F. Meyer, S. Nagarajan, A. Benkert, M. Bär, M. Blum, W. Yang, F. Reinert, C. Heske, L. Weinhardt, and M. Zharnikov, J. Phys. Chem. Lett. **5**, 4143 (2014).
[50] C.D. Cappa, J.D. Smith, K.R. Wilson, B.M. Messer, M.K. Gilles, R.C. Cohen, and R.J. Saykally, J. Phys. Chem. B **109**, 7046 (2005).
[51] E.A. Raymond and G.L. Richmond, J. Phys. Chem. B **108**, 5051 (2004).
[52] P. Jungwirth and D.J. Tobias, J. Phys. Chem. B **106**, 6361 (2002).
[53] N. Galamba, J. Phys. Chem. B **117**, 589 (2013).
[54] Y. Marcus, Chem. Rev. **109**, 1346 (2009).
[55] L.-Å. Näslund, D.C. Edwards, P. Wernet, U. Bergmann, H. Ogasawara, L.G.M. Pettersson, S. Myneni, and A. Nilsson, J. Phys. Chem. A **109**, 5995 (2005).

[56] J.D. Smith, C.D. Cappa, W.S. Drisdell, R.C. Cohen, and R.J. Saykally, J. Am. Chem. Soc. **128**, 12892 (2006).
[57] S.P.K. Koehler, Y. Ji, D.J. Auerbach, and A.M. Wodtke, Phys. Chem. Chem. Phys. **11**, 7540 (2009).
[58] S. Abujarada, H. AlSalem, U.K. Chohan, G.L. Draper, and S.P.K. Koehler, J. Chem. Phys. **145**, 184201 (2016).
[59] A.R. Bainbridge and W.A. Bryan, New J. Phys. **16**, 103031 (2014).
[60] H. Ye, J.M. Kienitz, S. Fang, S. Trippel, M. Swanwick, P.D. Keathley, L.F. Velásquez-García, G. Cirmi, G. Rossi, A. Fallahi, O.D. Mücke, J. Küpper, and F.X. Kärtner, in *19th Int. Conf. Ultrafast Phenom. 2014 Pap. 09WedP337* (Optical Society of America, 2014), p. 09.Wed.P3.37.
[61] L. Yang, X.-Y. Yu, Z. Zhu, T. Thevuthasan, and J.P. Cowin, J. Vac. Sci. Technol. Vac. Surf. Films **29**, 061101 (2011).
[62] E. Champenois, *CpBASEX* (https://github.com/e-champenois/CPBASEX).

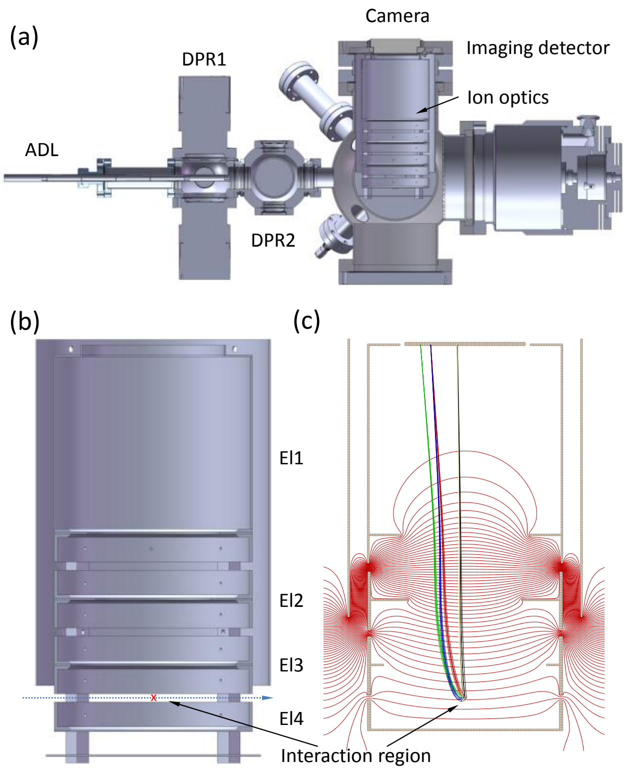

Figure 1. Scheme of the velocity-map imaging photoelectron spectrometer apparatus. a) Cross-section of the apparatus. ADL – aerodynamic lens; DPR1, DPR2 – differential pumping region 1 and 2. b) Cross-section of the VMI ion optics. El1 – El4 stand for electrodes 1 – 4. Blue dotted line depicts path of nanoparticles. Red cross corresponds to VUV/X-ray radiation perpendicular to the plane of figure. c) Simulation of ion optics (El1 = 0V, El = -5500 V, El3 = -7360 V, El4 = -8000 V). Red lines depict equipotential contours (going from -157 V on top to -7843 V in bottom). Colored lines, going from an interaction region towards a detector on top, depict trajectories of electrons emitted with kinetic energy of 60 eV at angles of 10, 50, 90, 130, and 170 degrees in respect to vertical axis of the VMI electron optics.

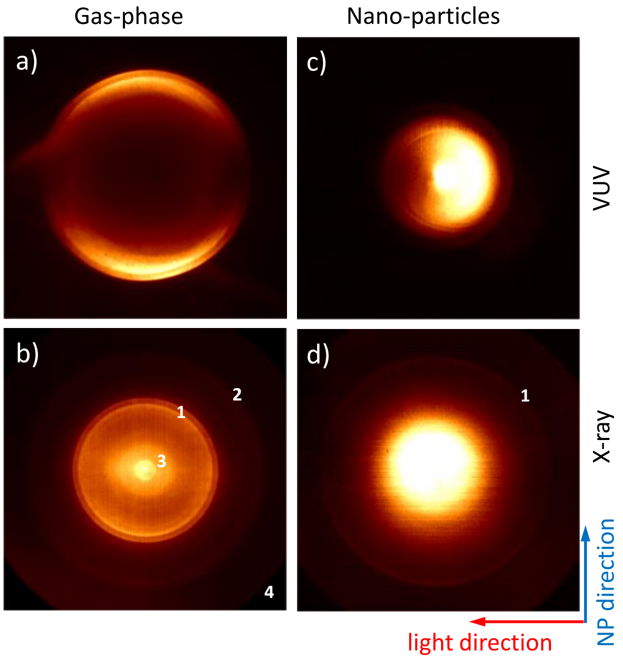

Figure 2. Velocity map images of gas-phase and nanoparticle samples: a) and b) depict spectra of gas-phase xenon measured at (a) 22 eV and (b) 80 eV photon energy. VMI spectra of squalene nanoparticles measured at (c) 15 eV and (d) 315 eV photon energy. The image feature labeled by 1 in panels (b) and (d) corresponds to photoelectrons. The dim ring labeled by 2 in panel (b) is due to emission of Auger electrons. Feature 3 corresponds to double Auger decay, and feature 4 depicts the edge of the imaging detector.

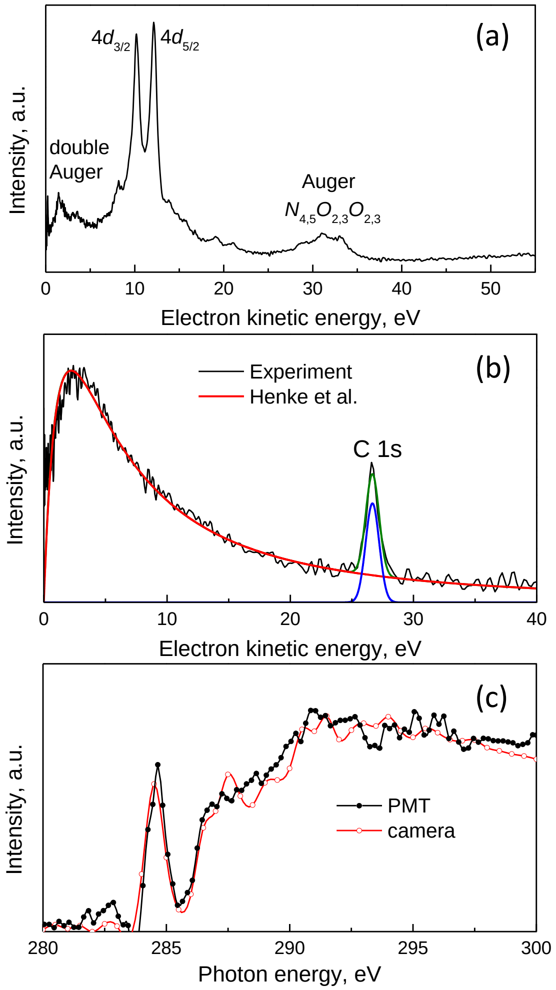

Figure 3. a) Reconstructed kinetic energy spectrum of xenon measured at photon energy of 80 eV. The spectrum corresponds to image shown in Figure 2b. b) Reconstructed photoelectron spectrum of squalene, obtained using photon energy of 315 eV. The corresponding image is shown in Figure 2d. The experimental data (black line) is fit using secondary electron model of Henke et al.[38] (red line). Photoelectrons are fit by a Gaussian function (blue line). The total signal is shown by the dark green line. c) NEXAFS spectrum of squalene measured with a PMT detector (black line and filled circles) and with a camera (red line and open circles).

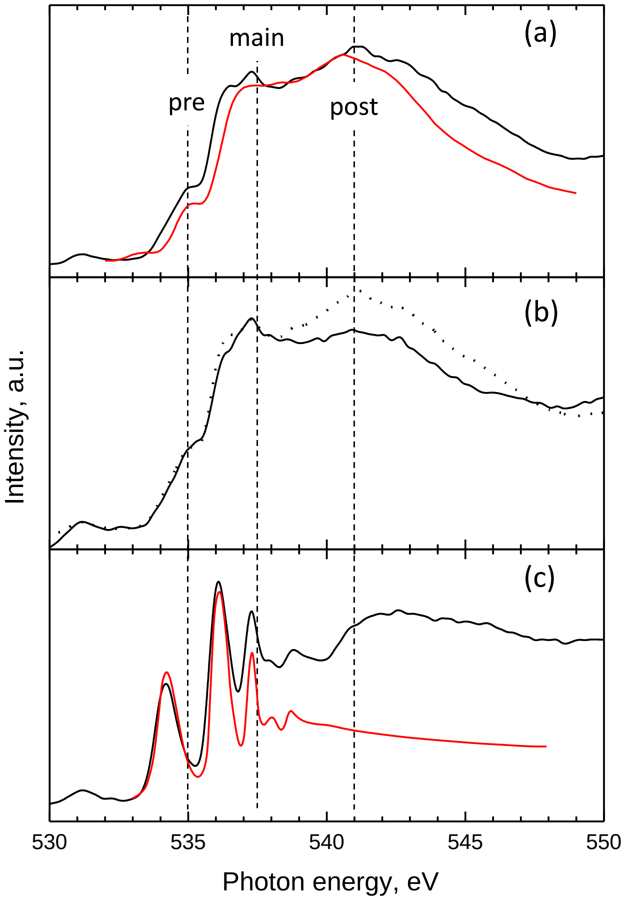

Figure 4. NEXAFS O 1*s* spectra (solid black lines) of a) nanoparticles generated from pure water, b) nanoparticles from 0.038 M solution of NaI in water (superimposed with the pure water data, shown by a dotted line), and c) gas-phase water. For comparison the spectra (a) composed of 40% liquid and 60% solid water NEXAFS and (c) gas-phase water are shown by red lines.[43] Dashed vertical lines depict positions of pre-, main-, and post-edges of water spectra observed in NEXAFS data.